Mechatronics 97 (2024) 103109

Contents lists available at ScienceDirect

Mechatronics

journal homepage: www.elsevier.com/locate/mechatronics

Actuator optimization and deep learning-based control of pediatric knee exoskeleton for community-based mobility assistance☆,☆☆

Sainan Zhang [a,b], Junxi Zhu [a], Tzu-Hao Huang [a], Shuangyue Yu [a], Jin Sen Huang [a], Ivan Lopez-Sanchez [a], Taylor Devine [c], Mohamed Abdelhady [c], Minghui Zheng [d], Thomas C. Bulea [c], Hao Su [a,e,*]

[a] Lab of Biomechatronics and Intelligent Robotics, Department of Mechanical and Aerospace Engineering, North Carolina State University, Raleigh, NC 27695, USA
[b] Department of Mechanical Engineering, City University of New York, City College, NY 10031, USA
[c] Rehabilitation Medicine Department, National Institutes of Health Clinical Center, Bethesda, MD 20892, USA
[d] Department of Mechanical and Aerospace Engineering, University at Buffalo, Buffalo, NY 14260, USA
[e] Joint NCSU/UNC Department of Biomedical Engineering, North Carolina State University, Raleigh, NC 27695, University of North Carolina at Chapel Hill, Chapel Hill, NC 27599, USA

ARTICLE INFO

Keywords:
Pediatric exoskeleton
Actuator optimization
Cerebral palsy
Deep learning

ABSTRACT

Lightweight and smart exoskeletons offer the potential to improve mobility in children. State-of-the-art pediatric exoskeletons are typically clinic-based since they are either tethered or portable but cumbersome and their design is often not optimized across a range of environments and users. To facilitate pediatric exoskeleton in community settings, we first proposed an actuator optimization framework that identified the optimal design parameters for both motor and transmission while minimizing the actuator mass and satisfying the output torque, speed, bandwidth, and resistance torque requirements. Guided by the optimization results, we customized a simple, lightweight actuator that met all mechatronic constraints for our portable exoskeleton (1.78 kg unilateral). Secondly, we adopted deep learning (Long Short Term Memory) based on gait phase estimation to facilitate stable control for community use. The models accurately estimated the gait phase on irregular walking patterns (accuracy 94.60%) without explicit training in children (typically developing and with cerebral palsy). The controller results demonstrated an elevated ability to adapt to the irregular gait patterns of the child with cerebral palsy. The experimental results in the child with typical development and four healthy adults demonstrated accurate assistive torque tracking performance (accuracy 97.00%) at different walking speeds (i.e., under uncertain torque to wearers). This work presented a holistic solution that includes both hardware innovation (actuator optimization framework) and software innovation (deep learning-based control) towards the paradigm shift of pediatric exoskeletons from clinic to community setting.

1. Introduction

Cerebral Palsy (CP) is a chronic health illness with the highest worldwide rehabilitation burden, according to the World Health Organization, due to its high prevalence, severity, and early onset. It is a disorder that limits mobility and reduces the quality of life [1]. Gait pathologies from CP cause inflated metabolic costs and decreased walking speed [2]. Pediatric exoskeletons have shown potential in improving the mobility of children with CP in clinic settings [3,4].

Pediatric wearable robots, based on their mechanical design, can be broadly classified into two groups: end-effector robots [4–7], and joint-based exoskeletons [3,8–10], as shown in Fig. 1. The end-effector robots are attached to users at one distal end, and the force generated at the distal interface influences the other joints. However, the robotic joints do not align with human joints, and isolating the movement of a single joint is challenging [5,6]. The joint-based exoskeletons ameliorate these limitations since they align with human knee joint axes [3,8,10].

☆ This paper was recommended for publication by Associate Editor Kyoungchul Kong.

☆☆ This work is supported in part by the National Science Foundation CAREER award CMMI 1944655, NSF Future of Work 2026622, Switzer Distinguished Fellow (SFGE22000372) of National Institute on Disability, Independent Living, and Rehabilitation Research (NIDILRR).

* Corresponding author at: Lab of Biomechatronics and Intelligent Robotics, Department of Mechanical and Aerospace Engineering, North Carolina State University, Raleigh, NC 27695, USA.
E-mail address: hao.su796@ncsu.edu (H. Su).

https://doi.org/10.1016/j.mechatronics.2023.103109
Received 7 July 2023; Received in revised form 29 October 2023; Accepted 22 November 2023
Available online 6 December 2023

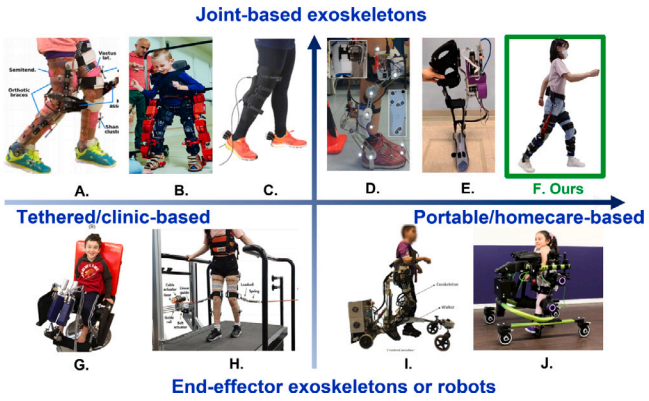

Fig. 1. Pediatric exoskeletons. Our (F) knee exoskeleton is the most lightweight of personal mobility devices. (A) NIH semi-tethered exoskeleton [3]. (B) ATLAS exoskeleton. (C) Soft material robot [11] (D) WAKE-Up exoskeleton [9]. (E) NIH portable exoskeleton [10]. (F) Our knee exoskeleton. (G) MIT pediatric robots [5]. (H) Cable-tensioning platform [6]. (I) HKAF Exoskeleton-Plus-Walker [4]. (J) Trexo robotics.

Furthermore, they enable the training of specific muscles and improve mobility by controlling the movement of the robot joints [10].

Although joint-based exoskeletons have shown great potential in clinical settings, the state-of-the-art joint-based pediatric exoskeletons are either tethered [3] or portable but cumbersome, heavy, and/or not compliant to natural human movement [9]. Soft material-based exoskeletons such as [11,12] are compliant but tethered. Therefore, to enhance mobility and independence in children with CP, the need for pediatric knee exoskeletons in community settings is becoming imperative and is a new frontier in wearable robots. To realize the objective of community-based pediatric rehabilitation, it requires a holistic solution that addresses the challenges in design (e.g., actuator optimization) and control (e.g., high-performance control).

The first challenge of community-based pediatric exoskeletons is individualized actuator design that satisfies multiple constraints. First, biomechanics, e.g., body mass, torque, and joint velocity, vary dramatically during child growth [13]. Second, multiple design constraints (typically conflicting) must be considered to satisfy children's kinematics and kinetics requirements [14]. For example, exoskeletons should provide sufficient torque while being lightweight and compliant (not impede natural movements). Third, the actuator mass should be as light as possible. Since the energetic penalty of walking increases proportionally with mass as a percentage of body weight, the extra weight brought by the exoskeleton can substantially increase the energetic cost of walking. Moreover, the influence of exoskeleton weight is more notable in children than adults due to their weight differences. The exoskeleton will alter the children's lower-limb kinematics if it exceeds the unilaterally mass 2.5 kg threshold [15]. Typically, it is considered that exoskeleton mass should not exceed 10% of the users' body mass. Recent interest has been in transmission optimization for actuators in exoskeletons (e.g., optimization of spring stiffness for series elastic actuation (SEA) [16]). There is no prior work on optimization of both motor and transmission for both series elastic actuators (with spring) and quasi-direct drive actuators (without spring) [17]. In addition, specialized methods guiding optimal actuator design accommodating child growth are also absent.

The second challenge in the community-based pediatric exoskeleton is the continuous phase controller to abrupt changes in gait. State-of-the-art controllers rely on the user's state to accurately time the assistance of the exoskeleton and can be classified into two groups: Finite State Machine (FSM)-based methods [18,19] and oscillator-based methods [20]. FSM-based methods rely on handcrafted transition rules based on accurately identifying discrete gait events such as heel-strike, toe-off, and swing phase. However, these methods are suitable only for steady-state walking, and may have difficulty adapting to changes in gait speed. On the contrary, oscillator-based methods continuously identify gait phases based on joint angles without relying on gait events. However, these methods suffer from delayed adaptation to the changes in gait speed, thus lacking the ability for *stride-by-stride* gait phase estimation, consequently hindering stability. Thus, state-of-the-art methods lack the ability towards abrupt changes in gait speeds and patterns, warranting the need for gradual changes in walking speeds to maintain stability [21,22], rendering them unsuitable for pediatric exoskeleton control for community use where such abrupt changes are commonplace. Recent advancements in deep learning offer promising solutions to learn complex nonlinear relationships commonly observed in kinematic data of human gait [21]. [23–25] demonstrated that deep learning could estimate hip gait phases or moments for healthy adults. Because their algorithms, inputted by inertial measurement units (IMUs), can capture the dominant motion of healthy adults in the sagittal plane during walking. However, children with cerebral palsy have non-sagittal plane movements, so it is still unknown whether deep learning for stable gait phase estimation for pediatric exoskeleton control is effective.

To enable the use paradigm of pediatric exoskeletons to shift from clinic to community settings, we proposed solutions to address the aforementioned two fundamental challenges in terms of actuator optimization and deep learning-based continuous phase controller. Firstly, we proposed a generalized method for optimizing actuators of exoskeletons to accommodate children of varying body masses. Our proposed method identified the optimal actuator design parameters for both motor and transmission while minimizing the actuator mass and satisfying the design requirements for output torque, speed, bandwidth, and backdrive torque. Guided by the optimization results, we customized a simple, lightweight actuator that met all mechatronic constraints for our portable exoskeleton, which is lightweight (1.78 kg unilateral), compliant, fully portable, and has a high bandwidth (40.3 Hz). Secondly, we developed a deep learning-based (LSTM) control method to improve the performance of exoskeletons in response to changes in gait speed. The proposed method accurately estimated the gait phase in abrupt changes in gait speed (with non-cyclic motion) without being explicitly trained on such data and also detected gait phases of children with cerebral palsy with non-sagittal plane motion. Furthermore, it automatically identified events of interest from raw inertial signals of the lower limbs, thus eliminating the need for cumbersome feature extraction and complex handcrafting of transition rules crucial for efficacy in commonly used finite-state machine-based controllers. Experiments with two children (one child with CP and one typically developing child) and four healthy adults show the effectiveness of the proposed method.

2. Mechatronics design of a portable pediatric knee exoskeleton

In this section, we present a lightweight and compliant pediatric knee exoskeleton (Fig. 2) based on the proposed actuation optimization method (Section 3). It illustrates an actuator design instance to demonstrate the feasibility and efficiency of the proposed user-specific optimization principles.

2.1. Mechanical design, electronics, and sensing system

Our exoskeleton comprises actuators, support frames for the thigh and shank, and a waist-mount system. To minimize mass and size, our transmission design uses simple planetary gears instead of complicated bevel gears [26] or chain mechanism [3]. The support frames fasten to limbs through cuffs with adjustable wearable straps. The 3D-printed cuffs and textile straps are adjustable to ensure a good fit for a large range of body dimensions. Two IMU sensors are worn on each leg, one on the thigh and one on the calf. One IMU sensor worn on the thigh was placed between the two thigh braces (middle thigh, sagittal plane)

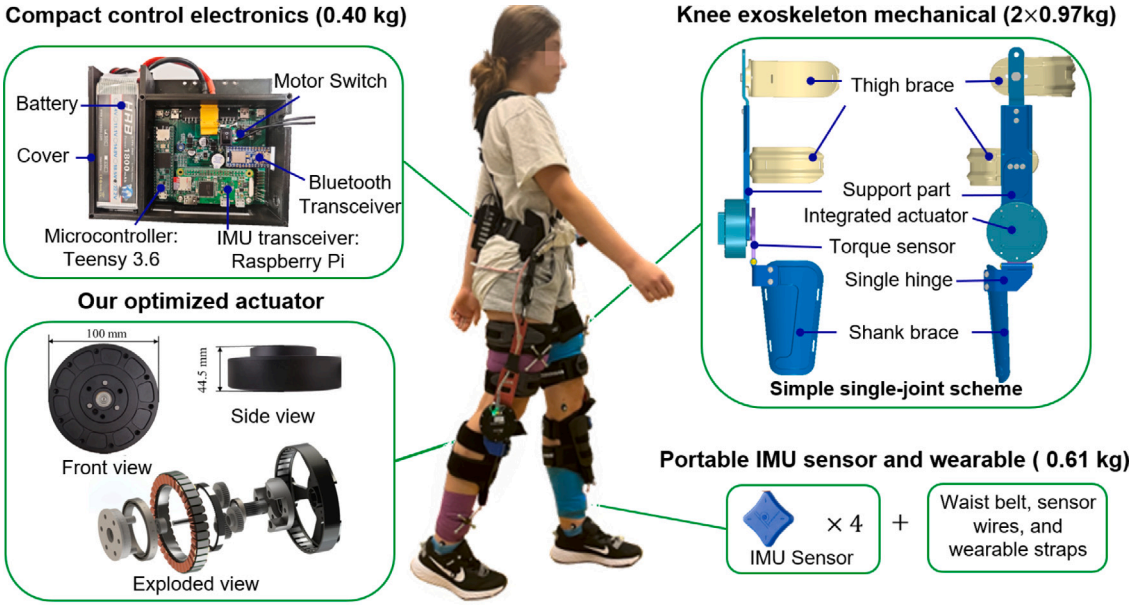

Fig. 2. Lightweight and portable pediatric knee exoskeleton for use in the community setting. It weighs 1.78 kg unilaterally (2.95 kg bilaterally) and incorporates compact control electronics, mechanical structures, inertial measurement unit (IMU) sensors (for gait detection), wearable structures, and batteries.

Table 1
Comparison of pediatric exoskeletons.

Pediatric exoskeleton	Unilateral mass (kg)	Actuator torque (N m)	Exoskeleton torque density (N m/kg)	Gear ratio	Actuator inertia[a] (kg cm^2)	Bandwidth (Hz)
MIT 2015	>10	7.21	Tethered system	138:1	105.50	Medium
NIH 2017 [3]	1.75[b]	16.10	Tethered system	311.5:1	537.56	Medium
NIH 2021 [10]	2.59	15.00	5.79	153:1	779.5	Medium (12)
NAU 2018 [2]	1.85	24.00	12.97	331:1	976.2	Medium
Ours (optimized)	**1.78**	**30.00**	**15.79**	**9:1**	**65.2**	**High (40.3)**

[a] Actuator inertia = Motor inertia × gear ratio^2.

[b] Semi-tethered system. It is the mass of the device brace and actuator. and [2] are pediatric ankle exoskeletons.

and at the thigh central axis (middle thigh, coronal plane). Another IMU sensor was placed between the bottom of the shank brace and the ankle (sagittal plane) for the calf. A customized torque sensor (resolution: ±0.1 N m, full scale: ±40 N m) measures the human–robot interaction torque and provides feedback for torque control. The customized torque sensor connects the optimized actuator to the shank support frame. A microcontroller (Teensy 4.1, 600 MHz) executes two outer loops of the three-stage controller hierarchy and handles the high-level walking control and mid-level PID torque control. Additionally, it communicates with the low-level current controller and encoder assemblies mounted on each actuator (Section 2.2) using the CAN bus protocol. A 14-bit magnetic rotary encoder is built into the actuator to measure the rotor's position, as well as an embedded microcontroller (STM32F407) that executes low-level motor control.

2.2. High torque density motor for optimized actuators

To serve our target population of 13–15-year-old children (45 ± 10 kg body mass), the proposed optimization framework (from Section 3) was used to design optimal actuators. Our customized actuator consists of a brushless DC motor with a gap radius of 0.039 m (3.3 N m peak torque) and a 9:1 planetary gear. It is powered by a nominal voltage of 48 V, enabling a peak output speed of 38.38 rad/s (nominal speed 26.17 rad/s) and 30 N m peak torque (11 N m nominal torque). The radial space resulting from a larger gap radius [27] was used to house the gearbox, which reduced the axial length of the actuator, thus making it compact. In addition, the small gear ratio significantly increased the compliance and bandwidth of the optimized actuator. Thus, the optimized actuator is more compact than our previous actuator [10,28]. Compared with the state-of-the-art pediatric exoskeletons in Table 1, the optimized exoskeleton has the highest torque density and smallest actuator inertia.

3. User-specific actuator optimization

To solve the challenges in actuator design of pediatric exoskeleton, this section formulated an optimization framework incorporating both motor and transmission design for SEA and quasi-direct-drive actuation paradigms [17]. The proposed optimization method can be generalized across exoskeleton size to enable the design of pediatric robots whose size requirements change with child growth and development. User-specific optimized actuator design is critical to maximizing the dynamics of the human–robot interaction. So, in this section, we introduced the details of actuator optimization in terms of the human–robot interaction model, geometric scaling laws, optimization constraints, and the results of actuator optimization.

3.1. Actuator design optimization framework

The proposed actuator design optimization framework is illustrated in Fig. 3, where the objective function (as shown in (1) and Fig. 3(B)) minimizes the actuator mass $m(r_g, n)$ to reduce the negative effect from exoskeleton mass with the optimization parameters, i.e., the motor gap radius r_g and the gear ratio n (as shown in Fig. 3(C)). Our optimization method considered multiple parameters (more than 10 parameters) as shown in Tables 3 and 4. Because many actuator parameters are related to (i.e., motor scaling laws) the motor gap radius and the gear ratio, our method also optimized multiple other actuator parameters (e.g., the moment of inertia J_m, the motor damping b_m, the motor

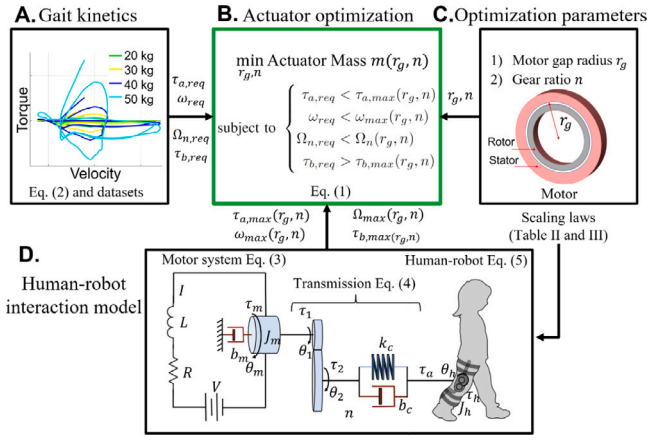

Fig. 3. Actuator optimization framework. (A) Pediatric gait kinetics of the knee. (B) Actuator optimization to minimize the actuator mechanical mass. (C) Optimization parameters: motor gap radius r_g and motor gear ratio n. (D) Human–robot interaction model. Tables 2 and 3 summarize the definitions of parameters.

Table 2
The nomenclature of the symbols in (1).

Symbols	Physical meaning
m	Actuator mass
r_g	Motor gap radius
n	Gear ratio
$\tau_{a,req}$	Required output torque of actuator
$\tau_{a,max}(r_g, n)$	Maximum output torque of actuator
ω_{req}	Required angular velocity of actuator
$\omega_{max}(r_g, n)$	Maximum angular velocity of actuator
$\Omega_{n,req}$	Required natural frequency under torque control
$\Omega_n(r_g, n)$	Natural frequency under torque control
$\tau_{b,req}$	Required backdrive torque of actuator
$\tau_{b,max}(r_g, n)$	Maximum backdrive torque of actuator

terminal resistance R, the motor terminal inductance L, the back EMF constant k_b via optimizing those two parameters.

The actuator optimization problem is formulated as follows

$$\underset{r_g,n}{\text{minimize}}\ m(r_g, n)$$

$$\text{subject to} \begin{cases} \tau_{a,req} < \tau_{a,max}(r_g, n) \\ \omega_{req} < \omega_{max}(r_g, n) \\ \Omega_{n,req} < \Omega_n(r_g, n) \\ \tau_{b,req} > \tau_{b,max}(r_g, n) \end{cases} \tag{1}$$

Since physical characteristics such as height and weight of children are vital for customizing exoskeleton systems, the constraints are selected based on the requirements of gait kinetics, shown in Fig. 3(A), and the dynamic human–robot interaction model Fig. 3(D). The gait kinetics is adopted to provide the torque $\tau_{a,req}$, angular velocity ω_{req}, natural frequency (bandwidth) $\Omega_{n,req}$ and backdrive torque $\tau_{b,req}$. The human–robot interaction model is proposed to illustrate the functions including $\tau_{a,max}(r_g, n)$, $\omega_{max}(r_g, n)$, $\Omega_{max}(r_g, n)$ and $\tau_{b,max}(r_g, n)$. With the output of the gait kinetics and kinematics ($\tau_{a,req}$, ω_{req}, $\Omega_{n,req}$ and $\tau_{b,req}$) and human–robot interaction model ($\tau_{a,max}(r_g, n)$, $\omega_{max}(r_g, n)$, $\Omega_{max}(r_g, n)$ and $\tau_{b,max}(r_g, n)$), the constraints can be formulated for the actuator optimization part (Fig. 3(B)). The rest of parameters are defined in Tables 2 and 3. Besides the mass of actuators, other alternative objective functions (e.g., energy consumption) are also feasible using this framework.

The required torque $\tau_{a,req}$ is body mass-specific and related to the peak knee moment. The peak knee moment comes from publicly available datasets of overground walking measured at self-selected walking

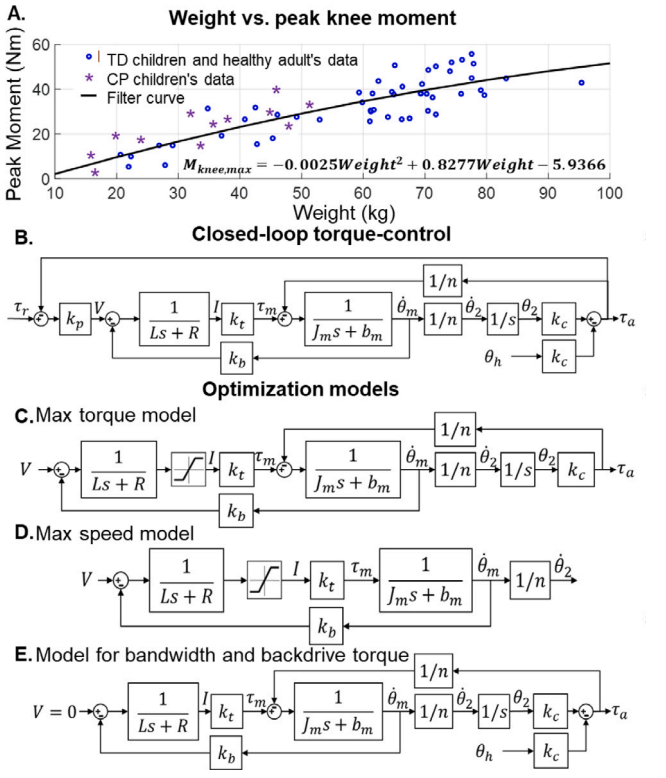

Fig. 4. (A) A quadratic curve to fit the peak knee moment at different body mass. The blue dots are the peak knee moments from [3,14,29] including data of 61 individuals. Block diagrams of (B) closed-loop torque control for the pediatric knee exoskeleton, (C) maximum torque, (D) exoskeleton maximum speed, (E) exoskeleton backdrive torque.

speeds for typically developing children [29], children with cerebral palsy [3,14]. The required angular velocity ω_{req} is set as 10.7 rad/s, corresponding to the maximum angular velocity. The natural frequency $\Omega_{n,req}$ is set as 20 Hz for human walking as required. The maximum backdrive torque $\tau_{b,max}$ of the unpowered exoskeleton in a walking cycle is 4 N m.

We proposed a quadratic curve (Fig. 4(A)) to fit the relationship between the age and knee moment $M_{knee,max}$, where the age for the adult dataset is set as 18. The fitted equation is formulated as

$$\begin{aligned} M_{knee,max} &= -0.0025Weight^2 + 0.8277Weight - 5.9366 \\ \tau_{a,req} &= 0.3M_{knee,max} \times 2 \end{aligned} \tag{2}$$

where the torque $\tau_{a,req}$ can be set as 50% of the peak knee extension moment with a safety factor of 2. User-specific optimized actuator design is critical to maximizing the dynamics of the human–robot interaction. So, in the remaining parts of this section, we introduced the details of actuator optimization in terms of the human–robot interaction model, geometric Scaling Laws, optimization constraints, and the results of actuator optimization. The proposed optimization framework can be generalized across exoskeleton size to enable the design of pediatric robots whose size requirements change with child growth and development.

3.2. Human-robot interaction model of torque control

Our optimization framework takes the human–robot interaction into consideration. The human–robot interaction model is given in Fig. 3(D). By comparing the open-loop bode plots between theoretical (Fig. 3(D)) and experimental results (open-loop frequency response of our exoskeleton), our proposed wearable robot model matches the experimental result with high accuracy. In Fig. 3(D), the human exoskeleton system consists of the electromechanical model of the actuator,

transmission, and human limbs. The quasi-direct drive actuator can be approximated as an equivalent electronic motor (consisting of a resistor, an inductance, and an ideal motor), motor's mechanical part, and a gearbox. The motor was modeled as

$$\begin{aligned} V &= LIs + RI + V_b, \\ V_b &= k_b\theta_m s, \\ \tau_m &= k_t I, \\ \tau_m &= J_m\theta_m s^2 + b_m\theta_m s + \tau_1, \end{aligned} \tag{3}$$

where the nomenclature included V winding voltage, V_b back electromotive force (EMF) voltage, k_b back EMF constant, k_t torque constant, L terminal inductance of the motor, R terminal resistance of the motor, I motor current, J_m moment of inertia of the rotor, θ_m motor angle, τ_m motor output torque, b_m motor damping coefficient, τ_1 gear input torque.

The gearbox is used to magnify the torque τ_1 by reducing the output angle. Therefore, we have

$$\theta_m = \theta_1 = n\theta_2, \quad \tau_2 = n\tau_1 \tag{4}$$

where θ_1 and θ_2 are the rotation angle of the input and output shaft, and τ_2 denotes the torque applied to the output shaft. The wearable structure of exoskeleton also serves as a transmission by transferring the actuator generated torque to the wearer. In our knee exoskeleton, this transmission includes braces, straps, and rigid linkages in our knee exoskeleton. The wearable structure is modeled as

$$\tau_2 = k_c(\theta_2 - \theta_h) + b_c(\theta_2 - \theta_h)s, \quad \tau_a = \tau_2 \tag{5}$$

where k_c is the human-exoskeleton transmission stiffness, b_c is the transmission damping factor, τ_a is the exoskeleton output torque, and θ_h is the human knee angle. By comparing the open-loop bode plots between theoretical (open loop transfer function) and experimental results (open-loop frequency response of our exoskeleton), our proposed wearable robot model matches the experimental result with high accuracy.

The block diagram of the torque control illustrated in Fig. 4(B) is implemented to assist human walking using the knee joint angles (Section 3.4). The input is the torque reference τ_r, and the output is the actual output torque τ_a applied to the human. Since the transmission damping coefficient b_c is small in practice, it can be set as zero. To investigate the torque control bandwidth, we set the input of the human knee angle θ_h to zero. The closed-loop transfer function of torque control is given by

$$\left.\frac{\tau_a(s)}{\tau_r(s)}\right|_{\theta_h(s)=0} = \frac{k_p k_c k_t n}{n^2 R J_m s^2 + n^2(Rb_m + k_b k_t)s + k_c(R + k_p k_t n)} \tag{6}$$

where k_p and k_i are proportional and integral control gains, respectively. The integral gain k_i is set as zero for simplicity, and winding inductance L is set as 0 for its negligible value.

The maximum angular velocity $\omega_{max}(r_g, n)$ can be obtained from the angular velocity ω, which is given by

$$\omega(s) = \frac{V k_t}{n(Rb_m + k_b k_t + (J_m R + L b_m)s + J_m L s^2)}. \tag{7}$$

The natural frequency Ω_n of closed-loop control is

$$\Omega_n = \sqrt{\frac{k_c(R + k_p k_t n)}{n^2 R J_m}}. \tag{8}$$

It is positively correlated with torque constant, and negatively correlated with gear ratio and moment of inertia.

The compliance is estimated from the backdrive torque, i.e., $\tau_b(r_g, n)$, under unpowered conditions. The block diagram is shown in Fig. 4(E). The input is human knee angle θ_h, and the output is the actuator output torque τ_b. With the motor voltage V set to zero, the transfer function can be reduced to

$$\left.\frac{\tau_b(s)}{\theta_h(s)}\right|_{V=0} = \frac{-k_c n^2 s[J_m R s + (Rb_m + k_b k_t)]}{n^2 s[J_m R s + (Rb_m + k_b k_t)] + R k_c}. \tag{9}$$

Table 3
The relationship between motor parameters and gap radius.

Symbols	Motor parameters	Relationship with gap radius (r_g)	Our optimized motor
r_g	Gap radius (m)	–	0.039
r_m	Motor radius (m)	$r_m \propto r_g$	0.048
M_m	Mass (kg)	$M_m \propto r_g$	0.566
J_m	Moment of inertia (kg m^2)	$J_m \propto r_g^3$	8.05E–6
b_m	Motor damping (N m s/rad)	–	0.01
k_t	Torque constant (N m/A)	$k_t \propto r_g$	0.232
k_b	Back EMF constant (V s/rad)	$k_b \propto r_g$	0.04
R	Terminal resistance (Ω)	$R \propto r_g^{-1}$	0.94
L	Terminal inductance (H)	$L \propto r_g^{-1}$	7.3E–4
V_{max}	Maximum voltage (V)	–	48
I_{max}	Maximum current (A)	$I_{max} \propto r_g$	7
τ_m	Motor torque (N m)	$\tau_m \propto r_g^2$	1.22
$\tau_{m,max}$	Maximum motor torque (N m)	$\tau_{m,max} \propto r_g^2$	3.33

As human motion is mostly low frequency ($\omega \to 0$) and the gear ratio n is small, the magnitude of $\left|\frac{\tau_b(s)}{\theta_h(s)}\right|_{s=j\omega}$ goes to zero with decreasing ω and n. Therefore, a system with lower frequency, smaller motor, and lower gear ratio produces lower backdrive torque and better compliance.

In summary, low backdrive torque and high natural frequency are the most critical requirements of an exoskeleton. However, there are trade-offs between these two: (1) maximizing the compliance requires a low gear ratio and a small motor with a low moment of inertia and damping coefficient; (2) maximizing the output torque requires a high gear ratio and a high torque constant; (3) maximizing the speed requires a low gear ratio and a low back-EMF constant. To form the basis of this optimization, we quantified the effect of motor size and gear ratio on the output torque, speed, bandwidth, and backdrive torque in the following subsection.

3.3. Geometric scaling laws for actuator optimization

In addition to the constraints brought forward by the dynamic human–robot interaction, the actuator's geometric features (i.e., scaling of elements) also play essential roles in the optimization problem. This subsection illustrates how the scaling laws of an actuator, specifically geometric factors of motors and gear ratio of the transmission, influence the optimization problem in terms of the actuator mass, torque, and torque density. It also further explains why we can select the motor gap radius r_g and the gear ratio n as the optimization parameters.

3.3.1. Geometry consideration of high torque density motors

The performance of a high torque density motor with a small moment of inertia can be described by the gap radius of the motor with fixed rotor and stator radial thickness. The relationship between the gap radius and the motor parameters is shown in Table 3, with the parameters of our prototype motor provided as a point of reference. From [27], we have

$$\tau_{m,max}(r_g) \propto r_g^2, \tag{10}$$

$$M_m(r_g) \propto r_g, \tag{11}$$

$$\frac{\tau_{m,max(r_g)}}{M_m(r_g)} \propto \frac{r_g^2}{r_g} = r_g. \tag{12}$$

These equations indicate that the maximum torque, mass, and torque density of a motor are all related to motor gap radius (r_g). Thus the torque density of a motor is not constant for motors with different dimensions, and therefore, the geometric factor (gap radius r_g) can be considered as a design variable.

Table 4
The relationship between motor performance and gear ratio.

Symbols	Motor parameters	Relationship with gear ratio (n)
$\tau_{a,max}$	Maximum output torque	$\tau_{a,max} \propto n$
$\dot{\theta}_{2,max}$	Maximum output speed	$\dot{\theta}_{2,max} \propto 1/n$
ω_{max}	Bandwidth	$\omega_{max} \propto 1/n$
$\tau_{b,max}$	Maximum backdrive torque	$\tau_{b,max} \propto 1/n$

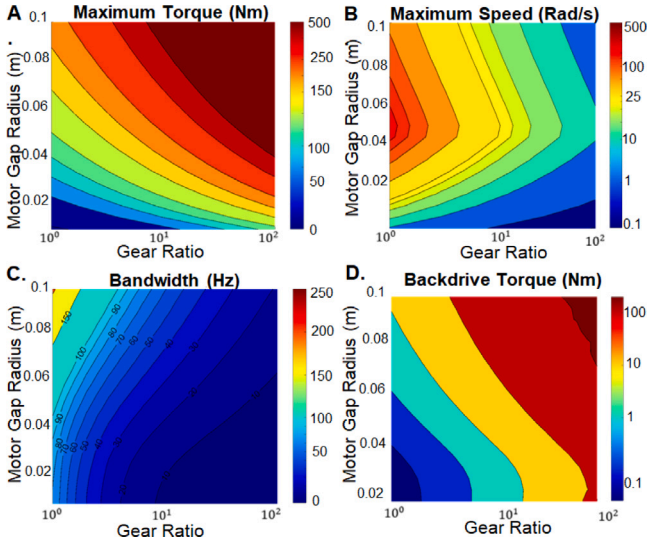

Fig. 5. Optimization constraints. (A) The maximum output torque with varied gear ratio and motor gap radius. The maximum torque increases when the gear ratio and the motor gap radius increase. (B) The maximum speed with varied gap radius and gear ratio. The maximum angular velocity is reached with the same gear ratio as the gap radius nears 0.05 m. The maximum angular velocity decreases with increasing of gear ratio. (C) High-frequency torque control requires a low gear ratio and high motor gap diameter. (D) Low resistance torque (high backdrivability) is ensured by a small motor gap diameter and low gear ratio.

3.3.2. Gear ratio consideration of the exoskeleton system

In this analysis, we assume that the gear ratio does not affect the mass of the actuator. This assumption is reasonable since the gearbox only makes up a minor part of the total mass of the actuator. From the results of Section 3.2, the relationship between motor performance and gear ratio is shown in Table 4. As the gear ratio increases, the output torque increases, while the output speed, bandwidth of torque control, and compliance decrease. The gear ratio of the transmission greatly affects the actuator performance. For this reason, we consider it as another core optimization parameter in our actuator design.

3.4. Optimization constraints

In this subsection, we elaborate on the four motor performance constraints for the actuation optimization problem: (1) maximum output torque, (2) maximum output speed, (3) bandwidth of torque control, and (4) backdrive torque.

3.4.1. Constraint of maximum output torque

To estimate the maximum output torque with respect to the gap radius and gear ratio, the block diagram in Fig. 4(C) is used to assume a fixed output angle.

We set the input voltage V as its maximum value $V_{max} = 48\,\text{V}$ and set the maximum output torque $\tau_{a,max}$ as the peak value of the output torque τ_a. The saturation current is set to I_{max} corresponding to the appropriate gap radius. Fig. 5(A) shows that maximum torque increases when gear ratio and gap radius increase. The $\tau_{a,max}(r_g, n)$ in (1) is obtained by finding the maximum output torque in Fig. 5(A) given a specific gap radius and gear ratio.

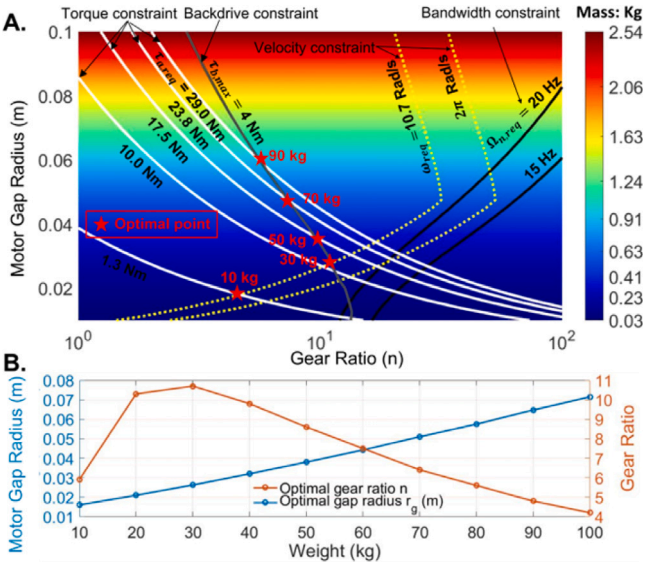

Fig. 6. Constraint contours in the optimization parameter space. The body mass-specific optimal solutions are found at the point that has the most negligible mass in the region bounded by the four constraint contours. (B) The optimal gap radius increases monotonically for children weighted from 10 kg to 100 kg, while the optimal gear ratio increases for weights between 10 and 30 kg and then decreases for weighted between 30 and 100 kg.

3.4.2. Constraint of maximum output speed

To estimate the maximum output velocity for different gap radii and gear ratios, we used the block diagram in Fig. 4(D) to assume a free output rotation. We set input voltage V as Fig. 5(B) illustrates that maximum angular velocity decreases as gear ratio increases. The maximum angular velocity is reached as gap radius nears 0.05 m, assuming constant gear ratio. The ω_{max} in (1) is obtained by finding the maximum output speed given a specific gap radius and gear ratio, as shown in Fig. 5(B).

3.4.3. Constraint of natural frequency of torque control

The bandwidth of torque control with different gap radii and gear ratios relies on the natural frequency. Natural frequency Ω_n from (8) is shown in Fig. 4(E), where $k_p = 1$. When the gap radius decreases and the gear ratio increases, the natural frequency decreases. $\Omega_n(r_g, n)$ in (1) is obtained by finding the bandwidth corresponding to a 1-Hz walking cycle in Fig. 5(C) given a specific gap radius and gear ratio.

3.4.4. Constraint of compliance

Average backdrive torque $\tau_{b,avg}$ is simulated by the block diagram in Fig. 4(E) and the result is shown in Fig. 5(D). The input is the knee angle trajectory θ_h at 1-Hz. As the gap radius and gear ratio increase, the backdrive torque increases. $\tau_{b,avg}(r_g, n)$ in (1) is obtained by finding the backdrive torque at 1 Hz in Fig. 5(D) given a specific gap radius and gear ratio.

3.5. Constrained optimization results

The objective function and constraint contours are plotted in Fig. 6(B). The minimum value is found in the area bounded by the four constraint contours. For example, the optimal solution for a 50-kg child lies at the intersection of the required torque contour ($\tau_{a,req} = 17.5$ N m) and the maximum backdrive torque contour ($\tau_{b,max} = 4$ N m). This leads to minimal actuator mass and the corresponding motor gap radius.

Finally, the body mass-related optimal result is shown in Fig. 6(B). The optimal motor gap radius monotonically increased from 0.017 to 0.072 m as the mass increased. The optimal gear ratio increased from

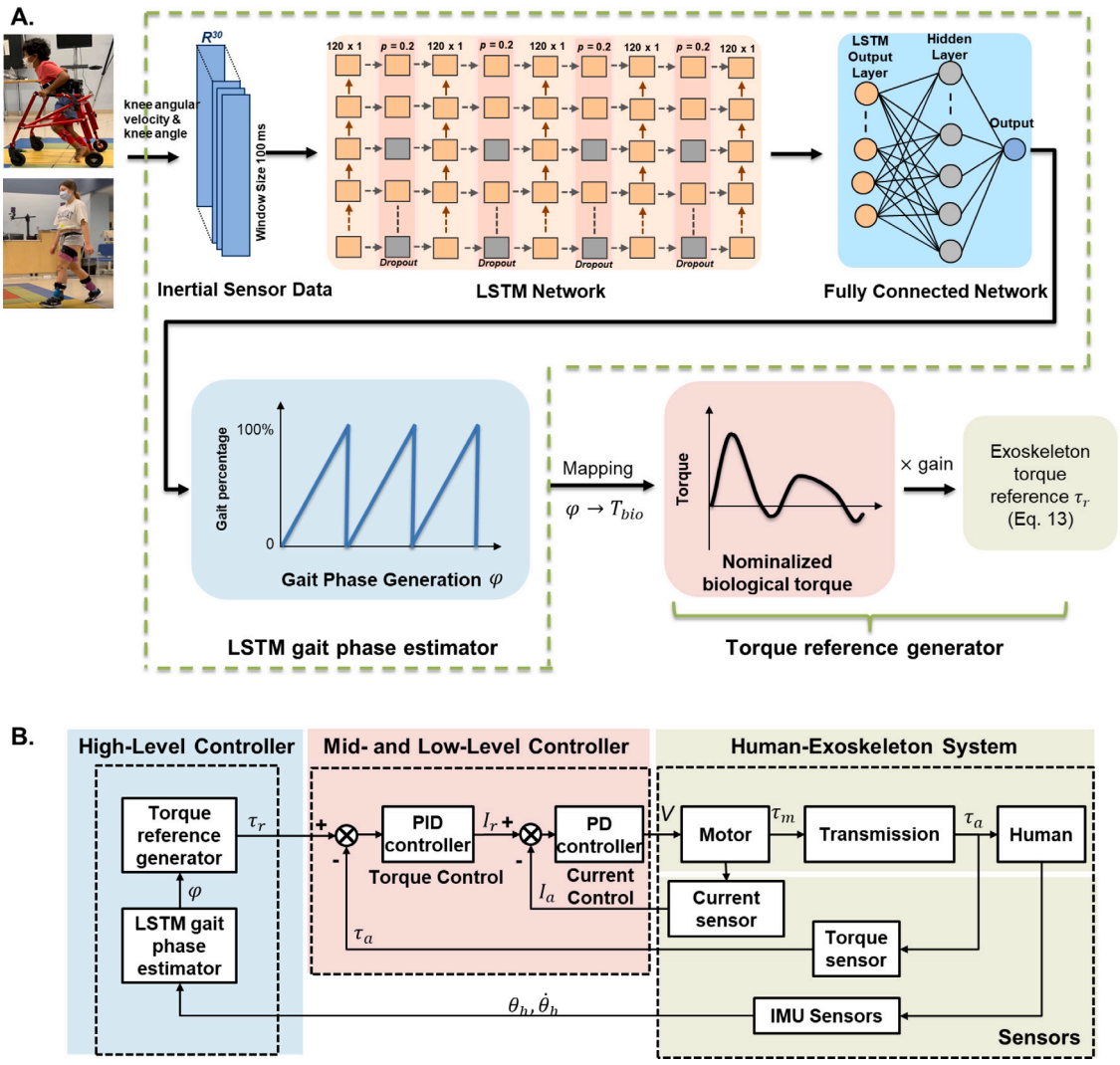

Fig. 7. (A) Long Short Term Memory (LSTM) networks for robust gait phase estimation during overground walking in children with CP and typically developing children. Linear acceleration and angular velocity from IMU sensors mounted on the thigh, shank, and pelvis were segmented in 100 ms or 200 ms windows with a step size of 1 and were used to train the LSTM model to estimate the gait phase. The predicted gait phase can then be used to generate appropriate assistive torque. The proposed method can be easily implemented in real-time. (B) Control diagram of torque controller for pediatric knee exoskeleton assistance. $\dot{\theta}_h$ and θ_h are knee angular velocity and angles measured by the IMU sensors in real-time.

5.9 : 1 to 10.8 : 1 as the body mass increased from 10 to 30 kg. The optimal gear ratio decreased from 10.8 : 1 to 4.2 : 1 as the weight increased from 30 kg. The decrease in optimal gear ratio was because the backdrive torque increased dramatically with the gear ratio (Fig. 6(B)). In summary, we demonstrated the principle of determining optimal exoskeleton design parameters for children of different weights by minimizing the actuator weight and satisfying the requirements for maximum torque, maximum speed, natural frequency, and backdrive torque.

4. Deep learning based gait phase estimation

Robustness to abrupt changes in gait speed is imperative for the efficacy of pediatric exoskeletons. Deep learning offers promise in improving the performance of pediatric exoskeleton controllers [26, 30]. However, these algorithms have not been explored for use in the pediatric population, especially in children with gait impairments due to cerebral palsy. Instead, these approaches have been limited to adults, prominently healthy individuals. Because the dominant motion of healthy adults in the sagittal plane during walking was well captured by these algorithms (IMUs' singles as inputs). Whereas children with cerebral palsy often have non-sagittal plane movements, it remains unknown as to whether deep learning algorithms for gait phase determination from IMUs are effective in this population.

The gait phase is a continuous state variable that represents the user's movement during the gait cycle. This variable is defined as a linearly increasing value between 0% and 100% (i.e., percentage of the gait cycle). By estimating the gait phase of the exoskeleton wearer in real-time, we can use the estimated gait phase φ to index the biological torque profile to produce the reference torque command in exoskeleton control. This study explored two state-of-the-art neural network architectures to estimate the gait phase, indicative of gait cycle progression and the onset of important gait events in typically developing children and children with CP.

4.1. Kinematic data collection of children with cerebral palsy

Deep learning is primarily a supervised learning approach. Thus, it relies on training datasets to map independent variables to dependent variables. Thus, we conducted human subject experiments involving one typically developing child and one child with CP to garner training datasets and assess the feasibility of using deep learning methods for

gait phase estimation in IMUs in the pediatric population. Force Sensitive Resistors' (FSR), commonly used in state-of-the-art Finite State Machine (FSM) based controllers, were not used because the efficacy of FSR's is affected by irregular contact patterns commonly observed in gait impairments and during community ambulation. Furthermore, they are sensitive to placement locations and are prone to performance degradation and failure over time [21,31]. Ground truth gait phases were labeled based on left heel strike data computed from the motion capture system for the typically developing child, whereas they were manually annotated for the CP child. Lastly, typically developing child experiments also yielded a test dataset of inertial signals representing abrupt changes in gait, simulating community setting, and was used to assess the effectiveness of trained models.

4.2. Deep neural network for robust gait phase estimation

A deep learning method was employed in this work called Long Short Term Memory Neural Networks (LSTM) primarily due to their inherent ability to extract features and capture historical events of interest automatically. Besides, its capabilities to perform gait phase estimation on non-mobility-impaired adults have been proven in similar works [25,32]. Thus, they facilitate an end-to-end learning paradigm that eliminates the need for manual and laborious feature engineering and the need for heuristic handcrafting of transition rules typically commonplace in FSM-based controllers [31]. Additionally, they enable stride-by-stride gait phase estimation and, thus, are more responsive than existing controllers that average over the past few strides, further improving stability.

4.2.1. LSTM-based gait phase estimator

LSTM networks are specifically designed to harness the underlying temporal relationship in sequential data effectively, as shown in Fig. 7(A). Its recurrent nature enables it to capture significant events from the input in the form of activation (short term), and efficient gradient-based algorithms enforce steady error flow through the network, resulting in accurate weight update (long term) [33]. This allows LSTM networks to capture nonlinear temporal relationships prominent in non-steady locomotion observed in community settings and individuals with gait impairment. The network consisted of 2 layers with a hidden state dimension of 30 and Tanh activation function. A dropout layer with 20% probability was added after each LSTM layer to facilitate generalizability. Lastly, a fully connected layer with 30 neurons was used to output the gait phase.

The input data (i.e., knee angular velocity and knee angle) consisting of raw inertial sensor data from the thigh, shank, and pelvis was normalized and structured in a window of 100 ms for the typically developing child and the child with CP with a step size of 1, and each window had a dimension of $\mathcal{R}^{30}$. To avert data leakage, which affects the validity of the trained network, the mean and standard deviation used to normalize training data were used to normalize the test data. The models were allowed to train for a maximum of 1000 epochs. However, the early stoppage was implemented to stop training due to a lack of improvement across multiple epochs and to prevent overfitting to promote generalizability. A 0.01 learning rate was used to train the models. The network weight and bias were updated using Root Mean Squared Error (RMSE) as the loss function and Adaptive moment estimation (Adam) as the optimization algorithm. The number of layers, hidden layer dimension, and learning rate were tuned using k-fold cross-validation ($k = 10$). Two sets of models were trained, one using typically developing child data and the other using CP child data. The typically developing child models were trained using 4 trials involving normal walking and were tested on trials involving abrupt changes in gait speed. The performance of CP children's models was evaluated via k-fold cross-validation to overcome the paucity of data yet assess a wide array of conditions. Secondarily, we also evaluated the accuracy of the leave-one-out set based on trials to ensure the reproducibility of k-fold validation results. Lastly, the Pearson correlation coefficient was used as the evaluation metric.

4.2.2. LSTM-based control strategy

The control strategy (as shown in Fig. 7(B)) in our pediatric exoskeleton is hierarchical, including a high-level control to generate assistive reference and a low-level control to track the torque reference. Human knee angles θ_h and angular velocity $\dot{\theta}_h$ are measured by inertial measurement units (IMUs), and these signals are used in our LSTM gait phase estimator to estimate the gait phase percentage φ in real-time. The estimated gait phase is used to index the biological torque profile to produce the reference torque reference τ_r:

$$\tau_r = A \times M_{biological}([\varphi]), 0 \leq \varphi \leq 100 \tag{13}$$

where A is the assistive toque gain (constant), $M_{biological}$ is the normalized biological knee joint moment.

4.3. State-of-the-art gait phase estimation methods

To understand and compare the effectiveness of our method and different gait estimation methods under abrupt gait pause and CP children's abnormal gait, this subsection introduces another deep learning method and a state-of-the-art none-machine-learning method: Convolutional Neural Networks (CNN) and oscillator gait estimation method [34,35].

4.3.1. CNN-based gait phase estimator

CNN is a regularized variant of a feed-forward neural network that optimizes the extracted features by applying convolution to the raw input signals during training. CNN is efficacious at automatically extracting inherent features from sequential data. Notes that, although CNN works well in estimating able-bodied gait phase, accurate and stable gait phase estimation for children with cerebral palsy is also to be explored. In this work, temporal relationships in sequential data, such as kinematic gait recordings, can be extracted by treating time as a spatial dimension. This architecture is known as 1D CNN, where the network convolves input sequences to capture significant events of interest across time. The network consisted of two 1D CNN layers with a ReLU activation function, and each layer consisted of 128 filters with a kernel size of 2. A max-pooling layer was added at the end of each 1D CNN layer to reduce the dimensions of the CNN layer and speed up the training process. The output of the second 1D CNN layer was flattened and fed to a fully connected layer with 50 neurons, which estimated the gait phase. Rectified Linear Unit (ReLU) was used as an activation function because various studies have established improved performance compared to Tanh. However, ReLU is not suitable for LSTM networks as the training may diverge due to large outputs.

4.3.2. Phase oscillator estimator

Phase oscillator estimator is a continuous gait phase measurement method that is parameterized by a mechanical variable from a single IMU sensing the human thigh motion. This method utilizes the relationship between thigh angle and speed (i.e., the thigh phase portrait) to construct the phase variable of the parameterized human gait cycle. As only a single sensor is used, the phase oscillator Estimation method can reduce the onboard calculation and equipment required to determine the gait phase. However, it lacks the ability to predict the gait of stopping and other mutations, and the effectiveness of this method in the gait detection of CP children needs to be explored.

5. Experiments and evaluation results

We conducted exoskeleton and human experiments with two objectives. First, we systematically evaluated the performance of the exoskeleton with the optimized actuator. Second, we acquired kinematic datasets necessary for training the deep learning models. One child (male, 7 years old, 109 cm, 18.1 kg) with cerebral palsy (GMFCS III), one typically developing child (female, 15 years old, 1.60 m, 51.3 kg), and four able-bodied adults (23.2 ± 2.8 years old, two

females and two males, 52.3 ± 3.6 kg, similar weight with target pediatric population) participated in our experiment. The experiments involving children were approved by the Institutional Review Board of the National Institutes of Health. The adult experiment was approved by the Institutional Review Board of North Carolina State University. All participants gave written informed consent prior to participation.

5.1. Evaluation of exoskeleton with optimized actuator

To evaluate the performance of the robot and ensure it satisfied our four optimization constraints, we tested the bandwidth (amplitude = 16 N m), compliance, and velocity tracking (max velocity = 10.7 rad/s) with our optimized pediatric exoskeleton. The results are shown in the supplementary video. Our exoskeleton has high bandwidth (40.2 Hz) for 16 N m torque magnitude, which is much higher than the state-of-art exoskeleton with 12 Hz [10], and the actuator meets the required output torque of actuator (15.6 N m for 45 kg). A higher bandwidth indicates our exoskeleton can handle children's highly dynamic daily movements. The Root mean square backdrive torque is only 0.30 N m in continuous 10 strides from a subject with the power-off exoskeleton (walking speed 1.0 m/s), suggesting that it has high compliance and does not restrict children's motion. The RMS velocity tracking error at 10.7 rad/s is 0.012 rad/s, meaning that our exoskeleton can accurately track the desired angular velocity profile and satisfy the varying walking speeds of children. Therefore, the systematic evaluation results demonstrated our exoskeleton with the optimized actuator satisfied the four optimization constraints well.

5.2. Evaluation of deep learning-based gait phase estimation

We recruited one typically developing child and one child with cerebral palsy to garner a training dataset and assess the feasibility of using deep learning methods for gait phase estimation in the pediatric population. Both subjects walked over a 6-meter walkway for at least 4 trials without any constraints on walking speed. The experiment involving the typically developing child included an additional condition where the subject was asked to stop in the middle of the walkway and resume walking to simulate the abrupt change in gait. Kinematic data was captured using an inertial motion capture system (Noraxon USA, Inc.). The Z-axis of each shank IMU sensor is aligned with the anteroposterior axis, and the Z-axis of each thigh sensor is aligned with the mediolateral axis. Lastly, one IMU sensor was attached to the posterior side of the waist.

To evaluate the three gait phase methods in terms of LSTM, CNN, and phase oscillator, the gathered data from this session was used in the three algorithms to perform the gait phase estimation task and assess their performance, as shown in Fig. 8. The evaluation primarily focused on assessing the ability of the three methods to estimate the gait phase given a sequence of data involving sudden pauses during walking (typically developing child) and high irregularities in the gait (child with CP). For deep learning models, the K-fold cross-validation revealed a high accuracy of 97.31% for both LSTM and CNN models.

Fig. 8(A) illustrates the gait phase estimation results under a typically developed child walking with abrupt pauses. The estimated gait phase of the LSTM model closely followed the actual gait phase with a high correlation coefficient (r) of 94.60%. The CNN network had similar performance with a correlation coefficient (r) of 94.51%. The high accuracy, despite the presence of abrupt changes in gait speed and pattern, highlights the feasibility of leveraging deep learning approaches for gait phase estimation in typically developing children. Furthermore, the fact that the models were not trained explicitly using data with abrupt changes yet had a high accuracy further highlights the generalizability and robustness of these methods. In contrast, the oscillator phase estimator (non-deep learning method) can accurately estimate the gait when walking, but this method cannot predict a sudden stop immediately and performs about 450-millisecond gait estimation delay when abrupt changes occur (resulting in r = 65.56%).

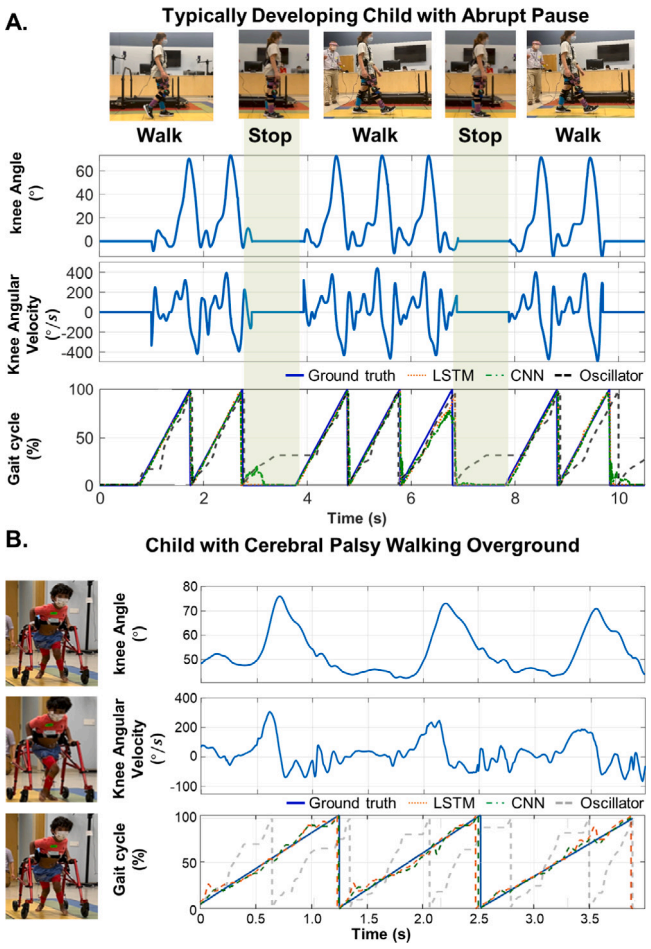

Fig. 8. Comparison results of three gait phase estimation methods. (A) Typically developing child with an abrupt pause. Deep learning methods (including both LSTM and CNN) can accurately estimate the gait cycle when abrupt changes occur. The estimated gait phase of LSTM and CNN closely followed the actual gait phase (ground truth) with a high correlation coefficient (r) of 94.60% and 94.51%, respectively. The oscillator phase estimator can accurately estimate the gait when walking, but this method performs about 450 ms gait estimation delay when abrupt changes occur (r = 65.56%). (B) Child with cerebral palsy walking overground. High accuracy gait phase estimation using LSTM compared to CNN in the child with cerebral palsy exhibiting severe crouch gait (GMFCS III). LSTM (r = 96.75%) performed slightly better than CNN (r = 95.12%). In contrast, the oscillator phase estimator failed to estimate this child's gait phase (r = 31.89%).

Fig. 8(B) shows the gait phase estimation results under a CP child overground walking. Regardless of severe gait impairment (GMFCS III) necessitating the use of a walking aid that resulted in highly varying gait patterns, the gait phase estimated by the LSTM model closely followed the actual gait phase (r = 95.35%), whereas the performance of the CNN model was comparatively higher (r = 97.60%). On the contrary, the accuracy of models on leave-one out of the set (train:4 trials, test:1 trial) showed that LSTM (r = 96.75%) performed slightly better than CNN (r = 95.12%). Lastly, these models are insensitive to the absolute value of the acceleration and velocity, and thus, minor misalignment between the IMU sensors and the human joint is tolerable. These results highlight the feasibility of deploying the trained models in real-time, which can be further simplified and accelerated through specialized packages such as MCUNet for microcontroller units. In contrast, the oscillator phase estimator failed to estimate this child's gait phase (r = 31.89%). The thigh angular velocity of the CP child has extra unnatural waves in a gait cycle, which mistakenly causes the

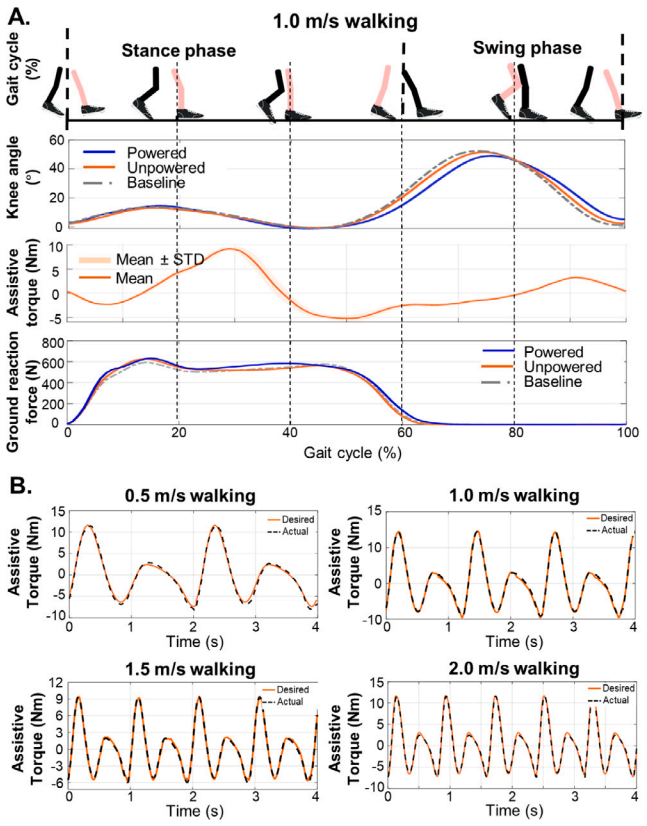

Fig. 9. (A) Kinematics and kinetics results. The exoskeleton demonstrated high compliance to movements with 94.7% similarity between maximum knee flexion angles during powered and baseline mode. Lastly, the low mass of the exoskeleton led to negligible effect on the user's kinetics as GRF during baseline and powered walking was 99.7%. (B) Torque tracking under different walking speeds. Our pediatric exoskeleton, using the optimized actuator, generated assistive torque with high accuracy (RMS error only 3.0%–4.6% of peak torque for 0.5–2.0 m/s walking speeds).

phase generated by the oscillator estimator to enter a new gait cycle. Therefore, these results demonstrated that deep learning methods can facilitate stable control for community use.

5.3. Human subject experiments

The human subject experiments aimed to evaluate the kinematics and kinetics impact of the exoskeleton during walking. Kinematics and kinetics were collected during continuous gait cycles from the typically developing child and four adult subjects (Fig. 9(A)). The kinematic observation (knee angles) illustrates that our lightweight pediatric exoskeleton induced minor changes in knee angle, which highlights the negligible exoskeleton mass penalty. The maximum knee flexion angle decreased by only 2.5 degrees during powered and baseline conditions (Pearson correlation coefficient = 0.947 ± 0.036). The maximum assistive torque generated by the exoskeleton is 7.5 N m for the child and 9.4 N m for adult subjects. Furthermore, we also analyzed the effect on the vertical ground reaction force (GRF) during walking. The mean GRF was lowered by only 0.17% during unpowered mode, whereas it increased by 4.4% during powered mode compared to baseline. The correlation between unpowered and baseline GRF was 98.93% and 99.7% between baseline and powered conditions. The negligible exoskeleton mass penalty on the kinematics and kinetics of the user highlights the efficacy of the exoskeleton with the optimized actuator. In the torque tracking experiments, subjects wore the powered pediatric knee exoskeleton and walked on a treadmill. Fig. 9(B) shows the accurate torque tracking of our exoskeleton under four different walking speeds (0.5 m/s, 1.0 m/s, 1.5 m/s, and 2.0 m/s). The torque tracking errors are only 4.6% (RMS error 0.53 ± 0.01 N m) at 0.5 m/s, 3.0% (RMS error 0.29 ± 0.01 N m) at 1.0 m/s, 3.7% (RMS error 0.44 ± 0.01 N m) at 1.5 m/s, and 3.9% (RMS error 0.45 ± 0.03) at 2.0 m/s. The torque error percentage is calculated by RMS error over the peak torque of desired torque $\tau_{d,p}$, i.e.,

$$\text{Error} = \frac{1}{\tau_{d,p}} \sqrt{\frac{1}{n} \sum_{i=1}^{n} (\tau_a(i) - \tau_d(i))^2} \times 100\%. \tag{14}$$

Therefore, the high torque tracking accuracy indicates synergistic control, demonstrating the ability to handle uncertainty due to variable walking speed.

6. Discussion and conclusion

We addressed hardware and control design challenges in pediatric exoskeletons tailored specifically for use in community settings. We proposed an optimization framework to enable a lightweight actuator design that satisfies the multifaceted requirements. In addition, we studied the feasibility of two deep learning methods for robust gait phase estimation for exoskeleton control in both typically developing children and children with cerebral palsy. The benchtop and human subject experiments involving the pediatric population characterized the effectiveness of our knee exoskeleton and demonstrated the functionality of our controller. Our results showed high compliance and accurate gait phase estimation and torque tracking in an adolescent-aged child. These features indicate the optimized exoskeleton is well-suited to alleviate excessive knee flexion in children with CP. Future studies will investigate our hypothesis that the optimized exoskeleton can increase the knee joint range of motion of children of CP with crouch gait to facilitate upright posture during walking. Future work will also include analysis of the exoskeleton margin of stability, as well as the dynamic stability of the user's gait during its use to support eventual use outside the clinical environment.

CRediT authorship contribution statement

Sainan Zhang: Methodology, Writing – original draft, Validation, Project administration. **Junxi Zhu:** Writing – original draft, Software. **Tzu-Hao Huang:** Methodology, Software. **Shuangyue Yu:** Writing – original draft, Validation, Resources. **Jin Sen Huang:** Validation, Investigation, Writing – review & editing. **Ivan Lopez-Sanchez:** Writing – review & editing. **Taylor Devine:** Writing – review & editing. **Mohamed Abdelhady:** Writing – review & editing. **Minghui Zheng:** Review & editing. **Thomas C. Bulea:** Writing – review & editing, Resources. **Hao Su:** Conceptualization, Supervision, Funding acquisition, Writing – review & editing.

Declaration of competing interest

The authors declare that they have no known competing financial interests or personal relationships that could have appeared to influence the work reported in this paper.

Data availability

Data will be made available on request.

Appendix A. Supplementary data

Supplementary material related to this article can be found online at https://doi.org/10.1016/j.mechatronics.2023.103109.

References

[1] Sadowska Małgorzata, Sarecka-Hujar Beata, Kopyta Ilona. Cerebral palsy: current opinions on definition, epidemiology, risk factors, classification and treatment options. Neuropsychiatr Dis Treat 2020;1505–18.

[2] Lerner Zachary F, Gasparri Gian Maria, Bair Michael O, Lawson Jenny L, Luque Jason, Harvey Taryn A, Lerner Andrea T. An untethered ankle exoskeleton improves walking economy in a pilot study of individuals with cerebral palsy. IEEE Trans Neural Syst Rehabil Eng 2018;26(10):1985–93.

[3] Lerner Zachary F, Damiano Diane L, Bulea Thomas C. A lower-extremity exoskeleton improves knee extension in children with crouch gait from cerebral palsy. Sci Transl Med 2017;9.

[4] Bayón Cristina, Martín-Lorenzo Teresa, Moral-Saiz Beatriz, Ramírez Óscar, Pérez-Somarriba Álvaro, Lerma-Lara Sergio, Martínez Ignacio, Rocon Eduardo. A robot-based gait training therapy for pediatric population with cerebral palsy: goal setting, proposal and preliminary clinical implementation. J Neuroeng Rehabil 2018;15(1):1–15.

[5] Michmizos Konstantinos P, Rossi Stefano, Castelli Enrico, Cappa Paolo, Krebs Hermano Igo. Robot-aided neurorehabilitation: a pediatric robot for ankle rehabilitation. IEEE Trans Neural Syst Rehabil Eng 2015;23(6):1056–67.

[6] Cho Seongyun, Lee Kun-Do, Park Hyung-Soon. A mobile cable-tensioning platform to improve crouch gait in children with cerebral palsy. IEEE Trans Neural Syst Rehabil Eng 2022.

[7] Marsi Bionics SL. Marci-bionic. Paediatric exoskeleton. 2020, https://www.marsibionics.com/en/atlas-pediatric.exo-pacientes/. Last accessed on 2023-04-20.

[8] Exoskeleton Report LLC. ATLAS paediatric exoskeleton. 2022, https://exoskeletonreport.com/product/atlas-2030/#. Last accessed on 2023-04-22.

[9] Patané Fabrizio, Rossi Stefano, Del Sette Fausto, Taborri Juri, Cappa Paolo. WAKE-up exoskeleton to assist children with cerebral palsy: design and preliminary evaluation in level walking. IEEE Trans Neural Syst Rehabil Eng 2017;25(7):906–16.

[10] Chen Ji, Hochstein Jon, Kim Christina, Tucker Luke, Hammel Lauren E, Damiano Diane L, Bulea Thomas C. A pediatric knee exoskeleton with real-time adaptive control for overground walking in ambulatory individuals with cerebral palsy. Front Robot AI 2021;8:173.

[11] Nguyen Pham Huy, Zhang Wenlong. Design and computational modeling of fabric soft pneumatic actuators for wearable assistive devices. Sci Rep 2020;10(1):1–13.

[12] Yang Xiaolong, Huang Tzu-Hao, Hu Hang, Yu Shuangyue, Zhang Sainan, Zhou Xianlian, Carriero Alessandra, Yue Guang, Su Hao. Spine-inspired continuum soft exoskeleton for stoop lifting assistance. IEEE Robot Autom Lett 2019;4(4):4547–54.

[13] De Ste Croix Mark BA, Deighan Martine A, Armstrong Neil. Assessment and interpretation of isokinetic muscle strength during growth and maturation. Sports Med 2003;33:727–43.

[14] van der Krogt Marjolein M, Sloot Lizeth H, Buizer Annemieke I, Harlaar Jaap. Kinetic comparison of walking on a treadmill versus over ground in children with cerebral palsy. J Biomech 2015;48(13).

[15] Rossi Stefano, Colazza Alessandra, Petrarca Maurizio, Castelli Enrico, Cappa Paolo, Krebs Hermano Igo. Feasibility study of a wearable exoskeleton for children: is the gait altered by adding masses on lower limbs? PLoS One 2013.

[16] Nieto Edgar A Bolívar, Rezazadeh Siavash, Gregg Robert D. Minimizing energy consumption and peak power of series elastic actuators: a convex optimization framework for elastic element design. IEEE/ASME Trans Mechatronics 2019;24(3):1334–45.

[17] Yu Shuangyue, Huang Tzu-Hao, Yang Xiaolong, Jiao Chunhai, Yang Jianfu, Chen Yue, Yi Jingang, Su Hao. Quasi-direct drive actuation for a lightweight hip exoskeleton with high backdrivability and high bandwidth. IEEE/ASME Trans Mechatronics 2020.

[18] Lewis Cara L, Ferris Daniel P. Invariant hip moment pattern while walking with a robotic hip exoskeleton. J Biomech 2011;44(5):789–93.

[19] Culver Steven, Bartlett Harrison, Shultz Amanda, Goldfarb Michael. A stair ascent and descent controller for a powered ankle prosthesis. IEEE Trans Neural Syst Rehabil Eng 2018;26(5):993–1002. http://dx.doi.org/10.1109/TNSRE.2018.2819508.

[20] Villarreal Dario J, Quintero David, Gregg Robert D. Piecewise and unified phase variables in the control of a powered prosthetic leg. In: 2017 international conference on rehabilitation robotics. 2017, p. 1425–30.

[21] Kang Inseung, Kunapuli Pratik, Young Aaron J. Real-time neural network-based gait phase estimation using a robotic hip exoskeleton. IEEE Trans Med Robot Bionics 2020;28–37.

[22] Huang Tzu-Hao, Zhang Sainan, Yu Shuangyue, MacLean Mhairi K, Zhu Junxi, Di Lallo Antonio, Jiao Chunhai, Bulea Thomas C, Zheng Minghui, Su Hao. Modeling and stiffness-based continuous torque control of lightweight quasi-direct-drive knee exoskeletons for versatile walking assistance. IEEE Trans Robot 2022;38(3):1442–59.

[23] Yang Jianfu, Huang Tzu-Hao, Yu Shuangyue, Yang Xiaolong, Su Hao, Spungen Ann M, Tsai Chung-Ying. Machine learning based adaptive gait phase estimation using inertial measurement sensors design of medical devices conference. Frontiers in biomedical devices, 2019, http://dx.doi.org/10.1115/DMD2019-3266.

[24] Camargo Jonathan, Flanagan Will, Csomay-Shanklin Noel, Kanwar Bharat, Young Aaron. A machine learning strategy for locomotion classification and parameter estimation using fusion of wearable sensors. IEEE Trans Biomed Eng 2021;68(5):1569–78.

[25] Molinaro Dean D, Kang Inseung, Camargo Jonathan, Gombolay Matthew C, Young Aaron J. Subject-independent, biological hip moment estimation during multimodal overground ambulation using deep learning. IEEE Trans Med Robot Bionics 2022;4(1):219–29.

[26] Lee Dawit, Kwak Eun Chan, McLain Bailey J, Kang Inseung, Young Aaron J. Effects of assistance during early stance phase using a robotic knee orthosis on energetics, muscle activity, and joint mechanics during incline and decline walking. IEEE Trans Neural Syst Rehabil Eng 2020;28(4):914–23.

[27] Wensing Patrick M, Wang Albert, Seok Sangok, Otten David, Lang Jeffrey, Kim Sangbae. Proprioceptive actuator design in the MIT cheetah: Impact mitigation and high-bandwidth physical interaction for dynamic legged robots. IEEE Trans Robot 2017;33(3):509–22.

[28] Yu Shuangyue, Huang Tzu-Hao, Di Lallo Antonio, Zhang Sainan, Wang Tian, Fu Qiushi, Su Hao. Bio-inspired design of a self-aligning, lightweight, and highly-compliant cable-driven knee exoskeleton. Front Hum Neurosci 2022;16:1018160.

[29] Chester Victoria L, Tingley Maureen, Biden Edmund N. A comparison of kinetic gait parameters for 3–13 year olds. Clin Biomech 2006;21(7):726–32.

[30] Yu Shuangyue, Yang Jianfu, Huang Tzu-Hao, Zhu Junxi, Visco Christopher J, Hameed Farah, Stein Joel, Zhou Xianlian, Su Hao. Artificial neural network-based activities classification, gait phase estimation, and prediction. Ann Biomed Eng 2023;1–14.

[31] Bae Jaehyun, Siviy Christopher, Rouleau Michael, Menard Nicolas, O'Donnell Kathleen, Geliana Ignacio, Athanassiu Maria, Ryan Danielle, Bibeau Christine, Sloot Lizeth, et al. A lightweight and efficient portable soft exosuit for paretic ankle assistance in walking after stroke. In: 2018 IEEE international conference on robotics and automation (ICRA). 2018, p. 2820–7.

[32] Kang Inseung, Molinaro Dean D, Duggal Srijan, Chen Yanrong, Kunapuli Pratik, Young Aaron J. Real-time gait phase estimation for robotic hip exoskeleton control during multimodal locomotion. IEEE Robot Autom Lett 2021;6(2):3491–7.

[33] Hochreiter Sepp, Schmidhuber Jürgen. Long short-term memory. Neural Comput 1997;9(8):1735–80.

[34] Quintero David, Lambert Daniel J, Villarreal Dario J, Gregg Robert D. Real-time continuous gait phase and speed estimation from a single sensor. In: 2017 IEEE conference on control technology and applications (CCTA). IEEE; 2017, p. 847–52.

[35] De La Fuente Juan, Subramanian Susheelkumar C, Sugar Thomas G, Redkar Sangram. A robust phase oscillator design for wearable robotic systems. Robot Auton Syst 2020;128:103514.

Sainan Zhang received B.S. degree in automatic from Xi'an University of Posts and Telecommunications, the M.S. degree in control science of engineering from the University of Electronic Science and Technology of China, Sichuan, China. She is currently working towards the Ph.D. degree supervised by Dr. Hao Su at the Department of Mechanical Engineering at the City University of New York, New York, USA. She is a visiting scholar in the Department of Mechanical and Aerospace Engineering at the North Carolina State University. Her current research interests include the control and optimization of lower-limb wearable robots.

Junxi Zhu received the B.S. from Shanghai Jiao Tong University and M.S. degree from the University of Maryland, College Park both in Mechanical Engineering. He is currently working towards a Ph.D. degree in the Department of Mechanical and Aerospace Engineering at the North Carolina State University, under the supervision of Professor Hao Su. His current research interest includes controller design and implementation of the exoskeleton system.

Tzu-Hao Huang received the B.S. degree in occupational therapy from National Cheng Kung University, Tainan, Taiwan, in 2004, the M.S. degree in the Institute of Rehabilitation Science and Technology from National Yang Ming University, Taipei, Taiwan, in 2006, and the Ph.D. degree in mechanical engineering from National Taiwan University, Taipei, Taiwan, in 2013. He is currently an assistant professor in the Department of Mechanical Engineering at the City College of New York. His major research area is control and design of the rehabilitation and assistive devices, humanmachine interface for assistive and rehabilitation device, brainmachine interface for subjects with movement disability, and the smart textile for physiological sensing in firefight, sport, and medical application.

Shuangyue Yu received the B.S. and M.S. degree from the Beijing University of Technology, Beijing, China, and the Ph.D. degree from the City University Of New York, City College. He is currently working as a postdoc supervised by Dr. Hao Su at the Department of Mechanical and Aerospace Engineering, North Carolina State University, Raleigh, USA. His current research interests include robot mechatronics, wearable robots and soft robots.

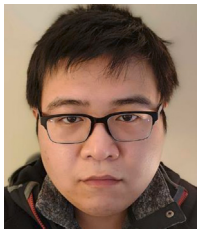

Jin Sen Huang received his Bachelor of Science in Mechanical Engineering in 2018 from North Carolina State University, Raleigh, NC. After spending two years working as an associate engineer for the Haas Formula 1 Team in Kannapolis, NC, he completed Master of Science in Mechanical Engineering in 2023 from North Carolina State University, Raleigh, NC. He is currently working towards a Ph.D. degree in Mechanical Engineering supervised by Dr. Hao Su at the Department of Mechanical and Aerospace Engineering at the North Carolina State University Raleigh, NC. His current research interests include mechatronic design of wearable systems and exoskeletons.

Ivan Lopez-Sanchez received the B.E. degree in aerospace engineering from Universidad Autónoma de Baja CaliforniaFCITEC, Tijuana, México in 2016 and the M.Sc. and Ph.D. degree in digital systems with specialization in control from Instituto Politécnico Nacional-CITEDI, Tijuana, México in 2019 and 2023, respectively. He is currently a Postdoctoral Research Scholar in the Biomechatronics and Intelligent Robotics Laboratory at the Department of Mechanical and Aerospace Engineering at the North Carolina State University Raleigh, NC. His research interests include nonlinear, robust, and intelligent control and its application to different mechatronic and robotic systems.

Taylor Devine received her Bachelor of Science in kinesiology from the University of Maryland in 2020. After spending two years working in a general surgery private practice, she completed a post-baccalaureate fellowship under Dr. Thomas Bulea at the National Institutes of Health in Bethesda, MD. Her research focused on adaptive technology for children with neuromuscular disorders. She is now a first-year medical student and Naval officer at the Uniformed Services University of the Health Sciences in Bethesda, MD.

Mohamed Abdelhady received his Ph.D. in electrical engineering from Cleveland State University and is currently a Postdoctoral fellow with the National Institutes of Health. Prior to this, he worked as a postdoctoral fellow at the Lerner Research Institute, Cleveland Clinic Foundation, Ohio, USA. He served as a research engineer with the Advanced Platform Technology Center (APT), Louis Stokes Cleveland Veterans Affairs (VA) Medical Center. Dr. Abdelhady has six years of industrial experience, with Ford Motor Co., MI, USA; Siemens R and D, Stuttgart, Germany; and Aramco Co., Jizan, Saudi Arabia. He is currently focused on combining advanced learning-based control with rehabilitation robots to create novel therapy tools and solutions for mobility disorders and paralysis.

Minghui Zheng received the B.E. and M.E. degrees, in 2008 and 2011 respectively, from Beihang University, Beijing, China, and the Ph.D. degree in Mechanical Engineering, in 2017, from University of California, Berkeley, USA. She joined University at Buffalo, NY, USA, in 2017, where she is currently an assistant professor in Mechanical and Aerospace Engineering. Her research interests include learning, planning, and control for multiple robotic systems such as collaborative manipulators for remanufacturing and drones for disaster resilience. She was the recipient of the NSF CAREER Award in 2021.

Thomas C. Bulea received the B.S. in mechanical engineering from The Ohio State University and M.S. and Ph.D. in biomedical engineering from Case Western Reserve University. He completed post-doctoral fellowships at the University of Houston and the National Institutes of Health Clinical Center. He joined the NIH Clinical Center in 2014 as a staff scientist and is currently a tenure track investigator in the Neurorehabilitation and Biomechanics Research Section of the Rehabilitation Medicine Department. Dr. Bulea's research interests include functional neuroimaging, neural interfacing, and rehabilitation robotics and exoskeletons for treatment of movement disorders. Dr. Bulea also serves as an Associate Editor of IEEE Transactions on Neural Systems and Rehabilitation Engineering and Wearable Technologies.

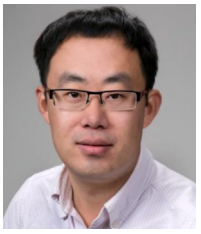

Hao Su is an Associate Professor in the Department of Mechanical and Aerospace Engineering at the North Carolina State University. He was Irwin Zahn Endowed Assistant Professor at City University of New York. He was a Research Scientist at Philips Research North America, and then a postdoctoral fellow at Harvard University and Wyss Institute for Biologically Inspired Engineering. Hao Su received B.S. degree from Harbin Institute of Technology, China, M.S. degree from State University of New York University at Buffalo, and Ph.D. degree from Worcester Polytechnic Institute. He serves as an associate editor of IEEE Robotics and Automation Letters (RAL), ASME Journal of Mechanisms and Robotics, IEEE International Conference on Robotics and Automation (ICRA), and IEEE/RSJ International Conference on Intelligent Robots and Systems (IROS).